ELECTROCHEMISTRY

A pyrolysis-free path toward superiorly catalytic nitrogen-coordinated single atom

Peng Peng[1]*, Lei Shi[1]*, Feng Huo[2]*, Chunxia Mi[1], Xiaohong Wu[2,3], Suojiang Zhang[2], Zhonghua Xiang[1]†

Nitrogen-coordinated single-atom catalysts (SACs) have emerged as a frontier for electrocatalysis (such as oxygen reduction) with maximized atom utilization and highly catalytic activity. The precise design and operable synthesis of SACs are vital for practical applications but remain challenging because the commonly used high-temperature treatments always result in unpredictable structural changes and randomly created single atoms. Here, we develop a pyrolysis-free synthetic approach to prepare SACs with a high electrocatalytic activity using a fully π-conjugated iron phthalocyanine (FePc)–rich covalent organic framework (COF). Instead of randomly creating Fe-nitrogen moieties on a carbon matrix (Fe-N-C) through pyrolysis, we rivet the atomically well-designed Fe-N-C centers via intermolecular interactions between the COF network and the graphene matrix. The as-synthesized catalysts demonstrate exceptional kinetic current density in oxygen reduction catalysis (four times higher than the benchmark Pt/C) and superior power density and cycling stability in Zn-air batteries compared with Pt/C as air electrodes.

INTRODUCTION

Carbon-based catalysts with nitrogen-coordinated single transition metal atoms as active sites have emerged as promising systems for catalytic processes because of their maximal atom utilization and highly catalytic activity (*1*–*8*). As revealed both experimentally and theoretically, the nitrogen-coordinated single transition metal moieties supported in carbon provide versatile active sites, while the carbon matrix ensures a large specific area and efficient mass transport, provides a stable matrix for the metal atoms, and affects the electronic density owing to strong intermolecular interactions (*9*–*16*). Currently, reported strategies to prepare the N-coordinated single-atom catalysts (SACs) dominantly depend on high-temperature pyrolysis, which highly demands the rigorous manipulation of the carbonization process and precise elemental ratio of precursors (*17*–*21*). For instance, during the pyrolysis of zeolitic imidazolate frameworks to prepare catalysts with single Fe-N-C sites, slight changes in pyrolysis temperature will lead to notable differences in catalytic performance (*22*–*25*). Meanwhile, because the isolated metal atoms are thermodynamically unstable, for many situations, the metal atoms tend to agglomerate as their ratio in precursors increases but hardly form single-atom centers when the ratio decreases (*14*, *26*). By this means, randomly creating Fe-N-C sites on the carbon matrix through pyrolysis is unpredictable and difficult to repeat in an atomic manner. There are many researches working on precisely tuning the nitrogen-coordinated SAC (*25*–*28*). However, developing precisely controllable synthesis of nitrogen-coordinated SACs in the long term for practical applications by means of high-temperature pyrolysis remains a challenge. To this end, we developed a pyrolysis-free synthetic approach SACs with a high electrocatalytic activity using a fully closed π-conjugated iron phthalocyanine (FePc)–rich covalent organic framework (COF).

[1]Beijing Advanced Innovation Center for Soft Matter Science and Engineering, State Key Laboratory of Organic-Inorganic Composites, Beijing University of Chemical Technology, Beijing 100029, P.R. China. [2]Beijing Key Laboratory of Ionic Liquids Clean Process, CAS Key Laboratory of Green Process and Engineering, State Key Laboratory of Multiphase Complex Systems, Institute of Process Engineering, Chinese Academy of Sciences, Beijing 100190, P.R. China. [3]University of Chinese Academy of Sciences, No. 19(A) Yuquan Road, Shijingshan District, Beijing 100049, P.R. China.
*These authors contributed equally to this work.
†Corresponding author. Email: xiangzh@mail.buct.edu.cn

RESULTS

Instead of randomly creating Fe-nitrogen moieties on the carbon matrix (Fe-N-C) through pyrolysis, we rivet the atomically well-designed Fe-N-C centers via intermolecular interactions between the Fe-N-C–rich pyrolysis-free COF network and the graphene matrix. Typically, as shown in Fig. 1A, we assembled benzene-1,2,4,5-tetracarbonitrile with Fe centers into a fully closed π-conjugated COF (termed COF_{BTC}) according to our previous method (*29*) to fabricate atomically dispersed Fe-N-C moieties (for additional details, see Materials and Methods), which were subsequently assembled with the graphene matrix via intermolecular interactions [see the extended x-ray absorption fine structure (EXAFS) and resistivity measurements discussed below]. Different from unpredictable pyrolysis, our single Fe-N-C centers were pre-assembled and directly riveted onto the graphene matrix; thus, the structures of the pyrolysis-free synthesized SACs (marked as *pf*SAC-Fe-X, where X represents the added mass ratio of COF_{BTC}) were well atomically arranged in the intact COF network. As expected, the graphene provided a stable matrix for the pre-assembled single Fe-N-C centers of COF_{BTC}. On the basis of the transmission electron microscopy (TEM) images (associated with elemental mapping), the as-obtained *pf*SAC-Fe demonstrated homogeneous elemental distribution (figs. S1 and S2), which was also confirmed by x-ray photoelectron spectroscopy (XPS) elemental analyses (fig. S3). We further performed atomic-resolution high-angle annular dark-field scanning transmission electron microscopy (HAADF-STEM) and identified that the coordinated Fe atoms, as represented by bright dots, were exclusively in the single-atom format and uniformly anchored throughout the graphene matrix (Fig. 1B and fig. S4).

The riveting of single Fe-C-N centers was successfully realized via the intermolecular interactions between the COF_{BTC} and the graphene matrix. As investigated by x-ray absorption fine structure (XAFS) spectroscopy, the Fe K-edge of x-ray absorption near-edge structure (XANES) of these specimens suggested that the *pf*SAC-Fe contained near-edge structures similar to those of the original FePc but totally different from those of the Fe foil (Fig. 1C), indicating a N-coordinated chemical state of single Fe atoms. In the Fourier transform analyses, the curve of *pf*SAC-Fe demonstrated a main peak belonging to the Fe-N scattering paths, while the Fe-Fe peak at about 2.2 Å

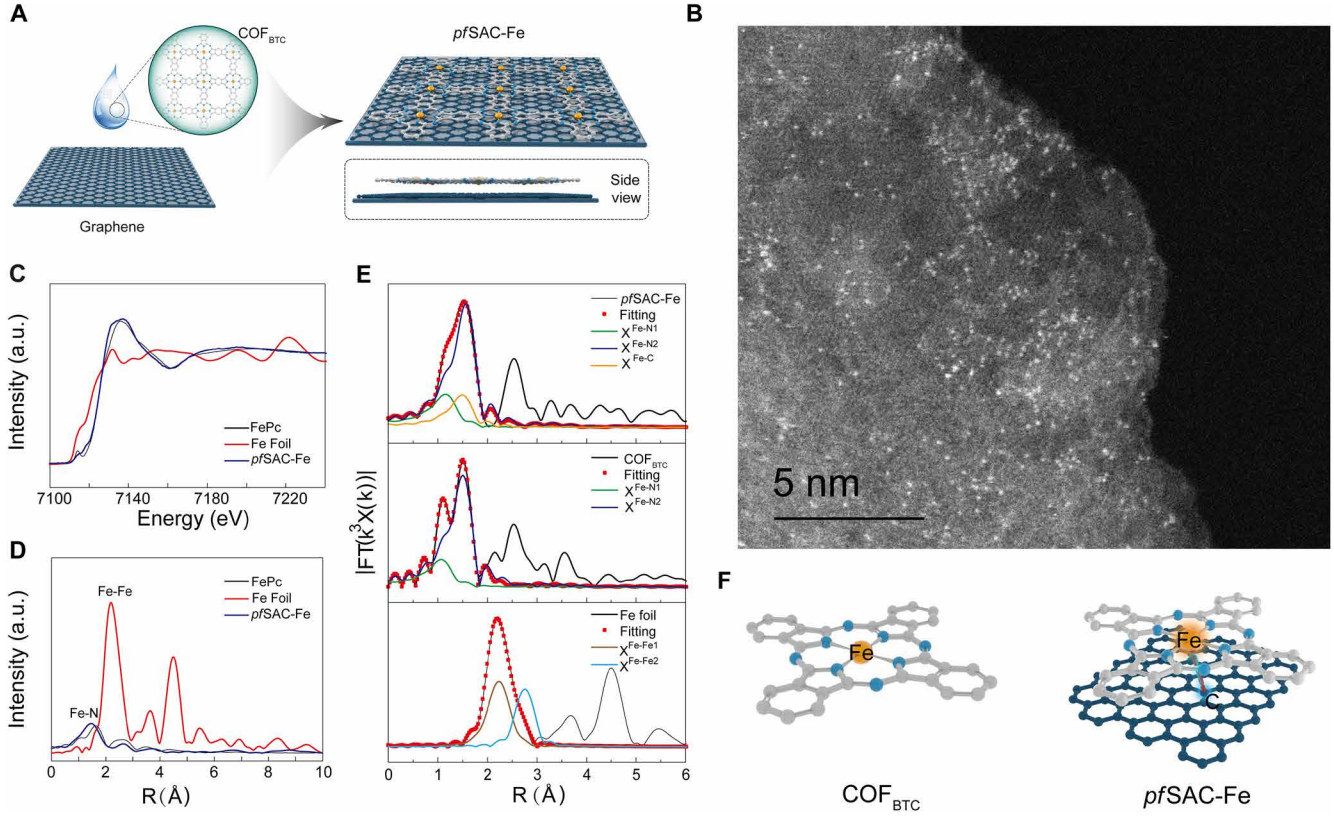

Fig. 1. Synthesis and structural characterization of *pf*SAC-Fe. (**A**) Synthesis route of the *pf*SAC-Fe catalyst. The intermolecular interactions are constructed during the process. (**B**) HAADF-STEM of the *pf*SAC-Fe-0.2. The graphene matrix is observed, on which plentiful Fe atoms (bright dots) are anchored. (**C** and **D**) Fe K-edge XANES spectra and Fourier transform (FT) of *pf*SAC-Fe-0.2, FePc, and Fe foil. a.u., arbitrary units. (**E**) Fe K-edge EXAFS analysis result in R spaces. The χ signals are the two-body backscattering paths of Fe-N, Fe-C, and Fe-Fe. (**F**) Simulated structures according to the Fe K-edge EXAFS analysis result.

was not detected (Fig. 1D). We further simulated the Fe K-edge EXAFS, finding the signals of the two-body backscattering path of Fe-N in both *pf*SAC-Fe and COF_{BTC} while Fe-C was uniquely formed in the *pf* SAC-Fe (Fig. 1E and figs. S5 to S7). Accordingly, only van der Waals interaction was observed during the electron localization function (ELF) analysis (Fig. 2A) with the density functional theory (DFT) calculations. As confirmed by the comparison of charge density differences, the electrons of graphene were attracted to the N-coordinated Fe sites, forming an Fe-C electron pathway (Fig. 2B). Moreover, once oxygen was introduced, we observed that it was only absorbed onto the single Fe atoms (Fig. 2C), which offered superiorly catalytic sites for the oxygen reduction reaction (ORR) (vide infra).

Similar to randomly creating Fe-N-C centers on the carbon matrix through pyrolysis, our approach to rivet the pre-assembled Fe-N-C onto graphene also generated a facile electron transfer environment. In the powder electrical resistivity measurement, we observed that once the intermolecular interactions were constructed, the resistivity of as-prepared *pf*SAC-Fe-0.2 decreased markedly, becoming very close to that of the raw graphene (Fig. 3A). By constructing the equivalent circuit based on the experimental data, we noted that the resistivity of the *pf*SAC-Fe-0.2 was in between the parallel connection and the series-parallel connection at low pressure (<12 MPa) while climbing higher than either the parallel connection or the series-parallel connection as the pressure increases (Fig. 3B). Because of the high pressing force leading to a much tighter connection and better conductivity, this phenomenon suggested that the intermolecular interactions generated an electrically conducting bridge between the Fe-N-C moieties and the graphene matrix, which was not as efficient as the conjugated systems indwelling the graphene, but still greatly benefitted electron transport. As observed from the density of state (DOS), the COF_{BTC} was a semiconductor with a small direct bandgap. With the intermolecular interactions with graphene, the *pf*SAC-Fe exhibited excellent electrical conductivity similar to metal, which prominently enhanced the charge transfer (fig. S12). Furthermore, the work function of *pf*SAC-Fe-0.2 obtained from the ultraviolet photoelectron spectroscopy (UPS) spectra in the valence band emission region was as small as 4.60 eV (Fig. 3C), suggesting a high driving force for donating electrons from the catalytic surface and facilitating the catalytic performance during ORR (*30*, *31*).

The electrocatalytic performance of *pf*SAC-Fe catalysts with different added ratios of COF_{BTC} was evaluated with a traditional three-electrode system. In cyclic voltammetry (CV) and linear sweep voltammetry (LSV) measurements with a rotating disk electrode, all of the *pf*SAC-Fe catalysts exhibited excellent catalytic performance for ORR compared to the benchmark Pt/C (Fig. 4A). In addition, the performance of *pf*SAC-Fe was enhanced with the increase in the added ratio of COF_{BTC}, demonstrating considerable high half-wave ($E_{1/2}$) potentials from 0.88 to 0.910 V versus reversible hydrogen electrode (RHE) (Fig. 4B). Meanwhile, the $E_{1/2}$ of the benchmark Pt/C was 0.86 V versus RHE, demonstrating the same activity as that in state-of-the-art literature (*32*–*34*). Consistent with the DFT

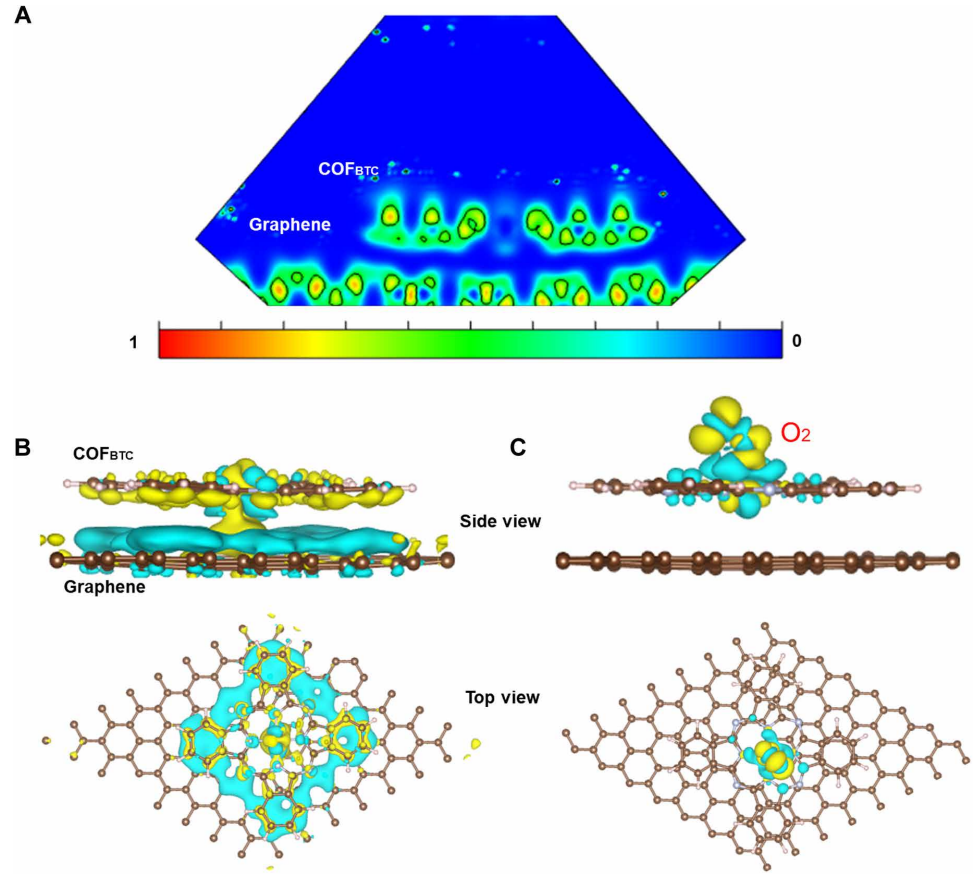

Fig. 2. Atomic structure analysis of *pf*SAC-Fe. (**A**) ELF of *pf*SAC-Fe. (**B**) Differential charge density distribution on *pf*SAC-Fe. (**C**) Differential charge density distribution on *pf*SAC-Fe with absorption of oxygen.

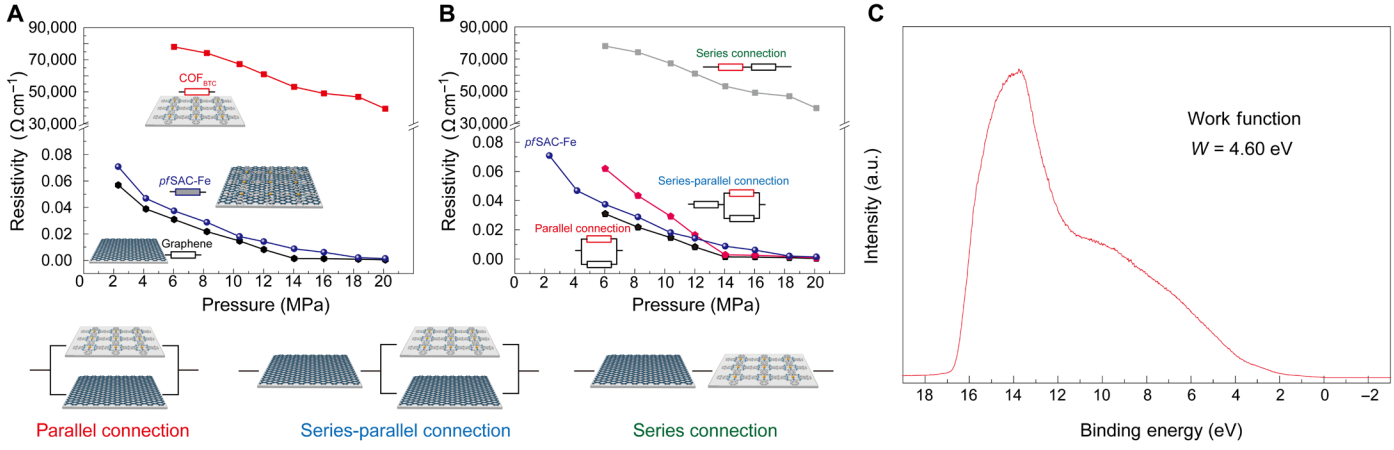

Fig. 3. Electronic conductivity studies. (**A**) The resistivity of COF_{BTC}, *pf*SAC-Fe-0.2, and pure graphene at different pressures. (**B**) The calculated equivalent circuit as series, parallel, and series&parallel connections compared with the *pf*SAC-Fe-0.2. Below: Schematic structures for series, parallel, and series&parallel connections. (**C**) The UPS spectra in the valence band emission region for *pf*SAC-Fe-0.2. The work function was calculated as 4.60 eV.

calculations, the single Fe atoms offered superior catalytic sites for the absorption and electron transfer of oxygen molecules during ORR. The optimized catalyst, *pf*SAC-Fe-0.2, exhibited the best ORR activity with a high kinetic current density (J_k) of 25.86 mA cm^{-2} at 0.85 V (versus RHE), which was about four times higher than that of Pt/C (6.49 mA cm^{-2}), and with a low Tafel slope of 31.7 mV $decade^{-1}$ (Fig. 4, B and C). The efficient kinetics were also confirmed by the Koutecky-Levich (K-L) plots and rotating ring disk electrode (RRDE) test, revealing a highly efficient four-electron pathway (3.85 to 4.0 per O_2) and a low H_2O_2 yield (below 7%) over 0.5 to 0.9 V (Fig. 4, D and E) (*35*). We also noted that the electrocatalytic performance, such as half-wave potential and kinetic current density,

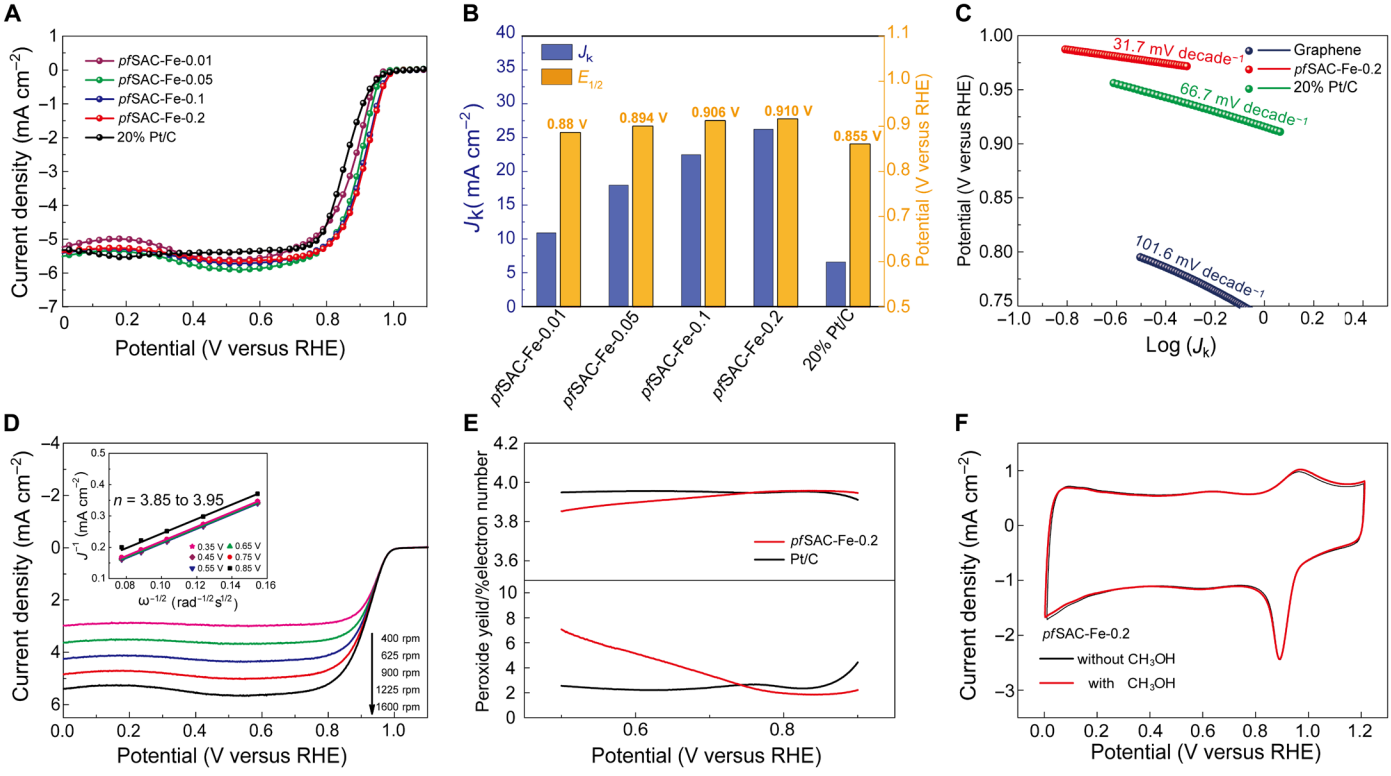

Fig. 4. Electrochemical characterization. (**A**) LSV curves of *pf*SAC-Fe-X and 20% Pt/C in O_2-saturated 0.1 M KOH solution at a scan rate of 5 mV s^{-1} and a rotation speed of 1600 rpm. (**B**) Kinetic current density (at 0.85 V versus RHE) and half-wave potentials of *pf*SAC-Fe-X and 20% Pt/C. (**C**) Tafel plots of graphene, *pf*SAC-Fe-0.2, and Pt/C. (**D**) LSV curves of *pf*SAC-Fe-0.2 at different rotation speeds. Inset: The corresponding K-L plots and electron transfer number. (**E**) H_2O_2 yields and electrode transfer number of *pf*SAC-Fe-0.2 and Pt/C in O_2-saturated 0.1 M KOH. (**F**) CV curves of *pf*SAC-Fe-0.2 in O_2-saturated 0.1 M KOH without and with 1.0 M methanol solutions.

was enhanced with increased catalytic loading (fig. S13), which was consistent with pioneering work (*36*, *37*). Superior to commercial Pt/C, the *pf*SAC-Fe catalysts exhibited better methanol tolerance during the methanol crossover test (Fig. 4F) and much longer durability during the continuous cycles (fig. S14A). The XAFS measurement of the *pf*SAC-Fe-0.2 test demonstrated similar curves after ORR tests, indicating that the structure of the catalysts was quite stable during the reaction (fig. S15). In addition, TEM and HAADF-STEM analyses confirmed that the single Fe atoms were still uniformly anchored throughout the graphene matrix after the ORR test (figs. S16 and S17).

Furthermore, in the homemade Zn-air battery with *pf*SAC-Fe-0.2 as the electrocatalysts for air cathode (Fig. 5A), we observed an open circuit potential as high as 1.41 V (Fig. 5B). Compared with the battery using conventional Pt/C as the electrocatalysts, the Zn-air battery driven by *pf*SAC-Fe-0.2 delivered similar discharge behaviors, higher power density (123.43 mW cm^{-2}, compared to 113.81 mW cm^{-2}, the power density of the battery driven by Pt/C), and larger specific capacity (732 mAh g_{Zn}^{-1} at 100 mA cm^{-2} with a zinc utilization of 89.3%) at the same loading (0.2 mg cm^{-2}) (Fig. 5, C and D). Besides, the Zn-air battery based on *pf*SAC-Fe-0.2 exhibited a notably long life cycle over 300 hours with a less than 0.1% decrease, suggesting the considerable stability of the *pf*SAC-Fe and the practical potential of the as-designed batteries, while the discharge voltage of the Pt/C-based system markedly decreased within 20 hours under the same conditions (Fig. 5E). We further periodically changed the current density from 5 to 40 mA cm^{-2} to evaluate the stability of cycle discharge performance and only observed a small voltage difference over 30 hours (Fig. 5F). Unexpectedly, even when the current density was as high as 100 mA cm^{-2}, the battery was still able to operate for more than 300 min with little potential drop (Fig. 5G). By increasing the loading of *pf*SAC-Fe catalysts to 0.5 mg cm^{-2}, the peak power density of the battery was raised up to 126.83 mW cm^{-2} (fig. S23), demonstrating a promising growth potential to replace the commercial Pt/C catalysts for metal-air batteries with high power density.

DISCUSSION

Rather than randomly creating single atoms on carbon through pyrolysis, we developed a pyrolysis-free synthetic approach to prepare SACs by riveting the pre-assembled COF_{BTC} on a conductive matrix (e.g., graphene) via intermolecular interactions. The as-synthesized *pf*SAC-Fe demonstrated a small work function and highly efficient catalytic performance for ORR. The Zn-air battery driven by the *pf*SAC-Fe exhibited superior power density and cycling stability for practical applications. The invented pyrolysis-free approach toward SACs not only paves a promising way to atomically optimize the SAC structures but also simplifies the accurate theoretical prediction calculations based on well-defined structures to develop more excellent catalysts for various energy conversions and storage devices (e.g., CO_2 reduction, N_2 fixation, and photoelectronic catalysis) besides oxygen reduction.

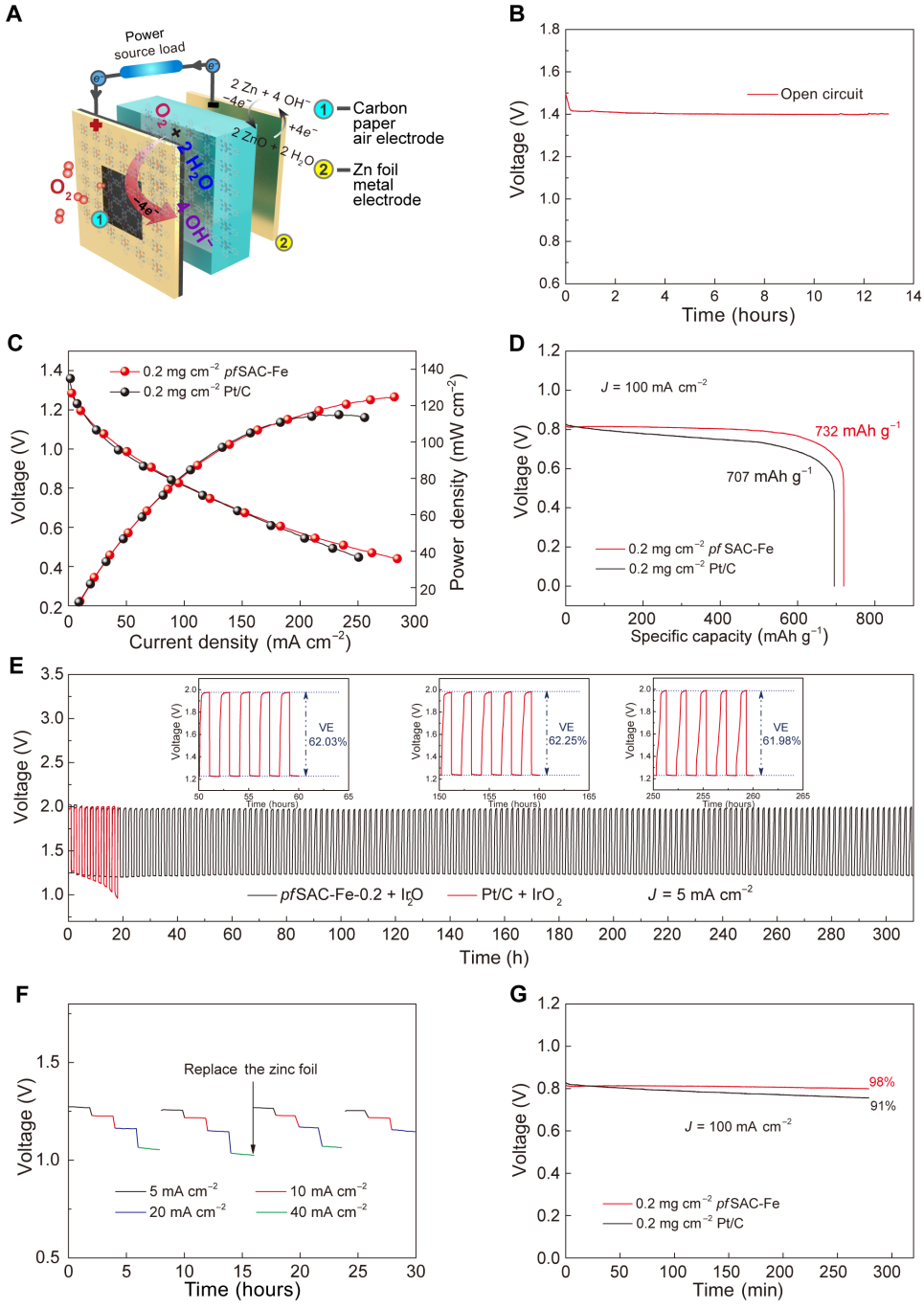

Fig. 5. Zn-air battery performance of *pf*SAC-Fe. (**A**) A schematic configuration of the homemade Zn-air battery. (**B**) Open circuit plot of the Zn-air battery using *pf*SAC-Fe-0.2 as catalyst. (**C**) Comparison of polarization and power density curves using Pt/C and *pf*SAC-Fe-0.2 as catalysts. (**D**) Comparison of specific capacities of the Zn-air batteries. (**E**) Long-term discharge/charge cycling performance of Zn-air batteries with Pt/C and *pf*SAC-Fe-0.2 as the ORR catalyst and IrO_2 as the oxygen evolution reaction catalyst at a current density of 5 mA cm^{-2}. Inset: Voltage efficiency (VE) of Zn-air batteries based on *pf*SAC-Fe-0.2 during the cycling test. (**F**) Cycle discharge curves of *pf*SAC-Fe-0.2–driven Zn-air batteries at periodically changed current densities of 5, 10, 20, and 40 mA cm^{-2}. (**G**) Discharge curves of Zn-air batteries using Pt/C and *pf*SAC-Fe-0.2 at current densities of 100 mA cm^{-2}. For each battery, a Zn plate was used as the anode, and 8 M KOH + 0.5 M ZnO was used as the electrolyte. All of the catalytic mass loading is at 0.2 mg cm^{-2}.

MATERIALS AND METHODS

Synthesis of *pf*SAC-Fe-X

To synthesize the *pf*SAC-Fe-X electrocatalysts, different mass ratios of as-synthesized COF_{BTC} (1, 5, 10, and 20%) were dispersed in glycol solution, followed by grinding with corresponding amounts of graphene. After grinding the mixture for 1 hour, the as-obtained composite material was kept in argon at 250°C to remove the glycol solvent. The as-prepared composite electrocatalysts were marked as *pf*SAC-Fe-X (X = 0.01, 0.05, 0.1, and 0.2, which represents the added mass ratios of the COF_{BTC}).

DFT calculation

We used the Vienna ab initio simulation package herein for all DFT calculations. To describe the interactions of the core electrons within different atoms, projected augmented wave was used. For exchange-correlation interactions, we adapted the generalized gradient approximation by Perdew-Burke-Ernzerhof. The plane wave basis sets had a cutoff energy of 500 eV to describe all atoms' valence electrons. The total energy of all the structures converged to 10^{-4} eV, and the Hellmann-Feynman force converged to 0.02 eV/Å. The Brillouin zone was set as the γ point. The graphene and COF_{BTC} were optimized separately before building the composite structure model, which was built by periodical single-layer graphene-based systems with a 15-Å vacuum to avoid the interactions between the layers. The lattice constants of these models were 19.7 Å by 19.7 Å by 15 Å. Van der Waals correction was applied in all composite structure calculations. ISPIN values were considered when calculating the models with magnetism.

Assembly of the Zn-air battery

Zn-air battery was assembled with homemade frameworks. On the air electrode, the catalysts were coated along with a gas diffusion layer at an effective size of 1.0 cm by 1.0 cm. A polished zinc foil was assembled as the negative electrode with the same effective size. The electrolyte was composed of 8 M KOH and 0.5 M ZnO. The battery performance was tested using a constant current charging-discharging process by Land Instruments at room temperature.

SUPPLEMENTARY MATERIALS

Supplementary material for this article is available at http://advances.sciencemag.org/cgi/content/full/5/8/eaaw2322/DC1

Supplementary Materials and Methods

Fig. S1. TEM images (associated with elemental mapping) of *pf*SAC, showing the existence and homogeneous distribution of C, Fe and N.

Fig. S2. TEM images (associated with elemental mapping) of pure graphene, in which no Fe and N was observed.

Fig. S3. XPS spectra and high-resolution XPS spectra of *pf*SAC-Fe-0.2.

Fig. S4. HAADF-STEM images of the *pf*SAC-Fe-0.2 sample.

Fig. S5. Fe K-edge EXAFS analysis of the Fe foil.

Fig. S6. Fe K-edge EXAFS analysis of pure COF_{BTC}.

Fig. S7. Fe K-edge EXAFS analysis of *pf*SAC-Fe-0.2.

Fig. S8. Relaxed structures for top-vertical absorption sites.

Fig. S9. Relaxed structures for top-horizontal absorption sites.

Fig. S10. Relaxed structures for bridge-horizontal absorption sites.

Fig. S11. Relaxed structures for bridge-vertical absorption sites.

Fig. S12. DOS for *pf*SAC-Fe and COF_{BTC}.

Fig. S13. The RRDE test using different *pf*SAC-Fe-0.2 loadings (from 40 to 304 μg cm^{-2}) in 0.1 M KOH.

Fig. S14. Stability tests for *pf*SAC-Fe-0.2.

Fig. S15. The Fe K-edge XANES spectra of *pf*SAC-Fe-0.2 before and after ORR.

Fig. S16. TEM images (associated with elemental mapping) of the *pf*SAC-0.2 sample after 6000 cycles of CV test, showing the homogeneous distribution of C, Fe, and N.

Fig. S17. HAADF-STEM images of the *pf*SAC-Fe-0.2 sample after 6000 cycles of CV test.

Fig. S18. CVs, H_2O_2 yields, and electron transfer number of *pf*SAC-Fe-0.01, *pf*SAC-Fe-0.05, *pf*SAC-Fe-0.1, and *pf*SAC-Fe-0.2.

Fig. S19. LSV curves of graphene, *pf*SAC-Fe-0.2, and 20% Pt/C in O_2-saturated 0.1 M KOH solution at a scan rate of 5 mV s^{-1} and a rotation speed of 1600 rpm.

Fig. S20. Kinetic current density of *pf*SAC-Fe-0.01, *pf*SAC-Fe-0.05, *pf*SAC-Fe-0.1, *pf*SAC-Fe-0.2, Pt/C, and graphene over 0.82–1.0 V versus RHE.

Fig. S21. LSV curves and the corresponding K-L plots of *pf*SAC-Fe-0.01, *pf*SAC-Fe-0.05, and *pf*SAC-Fe-0.1.

Fig. S22. Tafel plot and methanol crossover tests of the samples.

Fig. S23. Polarization and power density curves of assembled Zn-air batteries using Pt/C and *pf*SAC-Fe-0.2 as ORR catalysts with different loading masses.

Table S1. Fe K-edge EXAFS curve fitting parameters.

Table S2. Comparison of the ORR activity between *pf*SAC-Fe-0.2 and other nonprecious catalysts under basic conditions (0.1 M KOH) in literature.

Table S3. Inductively coupled plasma atomic emission spectroscopy results for Fe contents in COF_{BTC} and the as-obtained *pf*SAC-Fe-0.2.

Table S4. Comparison of the performance of the zinc-air batteries based on *pf*SAC-Fe-0.2 and other electrocatalysts.

References (*38*–*53*)

REFERENCES AND NOTES

1. H. T. Chung, D. A. Cullen, D. Higgins, B. T. Sneed, E. F. Holby, K. L. More, P. Zelenay, Direct atomic-level insight into the active sites of a high-performance PGM-free ORR catalyst. *Science* **357**, 479–484 (2017).
2. G. Kyriakou, M. B. Boucher, A. D. Jewell, E. A. Lewis, T. J. Lawton, A. E. Baber, H. L. Tierney, M. Flytzani-Stephanopoulos, E. C. H. Sykes, Isolated metal atom geometries as a strategy for selective heterogeneous hydrogenations. *Science* **335**, 1209–1212 (2012).
3. W. G. Liu, L. L. Zhang, X. Liu, X. Y. Liu, X. F. Yang, S. Miao, W. T. Wang, A. Q. Wang, T. Zhang, Discriminating catalytically active FeN_x species of atomically dispersed Fe-N-C catalyst for selective oxidation of the C-H bond. *J. Am. Chem. Soc.* **139**, 10790–10798 (2017).
4. H. Yan, H. Cheng, H. Yi, Y. Lin, T. Yao, C. L. Wang, J. J. Li, S. Q. Wei, J. L. Lu, Single-atom Pd-1/graphene catalyst achieved by atomic layer deposition: Remarkable performance in selective hydrogenation of 1,3-butadiene. *J. Am. Chem. Soc.* **137**, 10484–10487 (2015).
5. H. Yan, Y. Lin, H. Wu, W. H. Zhang, Z. H. Sun, H. Cheng, W. Liu, C. L. Wang, J. J. Li, X. H. Huang, T. Yao, J. L. Yang, S. Q. Wei, J. L. Lu, Bottom-up precise synthesis of stable platinum dimers on graphene. *Nat. Commun.* **8**, 1070 (2017).
6. M. Yang, S. Li, Y. Wang, J. A. Herron, Y. Xu, L. F. Allard, S. Lee, J. Huang, M. Mavrikakis, M. Flytzani-Stephanopoulos, Catalytically active Au-O(OH)(x)-species stabilized by alkali ions on zeolites and mesoporous oxides. *Science* **346**, 1498–1501 (2014).
7. X. F. Yang, A. Q. Wang, B. T. Qiao, J. Li, J. Y. Liu, T. Zhang, Single-atom catalysts: A new frontier in heterogeneous catalysis. *Acc. Chem. Res.* **46**, 1740–1748 (2013).
8. L. Yang, D. J. Cheng, X. F. Zeng, X. Wan, J. L. Shui, Z. H. Xiang, D. P. Cao, Unveiling the high-activity origin of single-atom iron catalysts for oxygen reduction reaction. *Proc. Natl. Acad. Sci. U.S.A.* **115**, 6626–6631 (2018).
9. C. W. B. Bezerra, L. Zhang, K. C. Lee, H. S. Liu, A. L. B. Marques, E. P. Marques, H. J. Wang, J. J. Zhang, A review of Fe–N/C and Co–N/C catalysts for the oxygen reduction reaction. *Electrochim. Acta* **53**, 4937–4951 (2008).
10. H. L. Fei, J. C. Dong, Y. X. Feng, C. S. Allen, C. Z. Wan, B. Volosskiy, M. F. Li, Z. P. Zhao, Y. L. Wang, H. T. Sun, P. F. An, W. X. Chen, Z. Y. Guo, C. Lee, D. L. Chen, I. Shakir, M. J. Liu, T. D. Hu, Y. D. Li, A. I. Kirkland, X. F. Duan, Y. Huang, General synthesis and definitive structural identification of MN_4C_4 single-atom catalysts with tunable electrocatalytic activities. *Nat. Catal.* **1**, 63–72 (2018).
11. W. J. Jiang, L. Gu, L. Li, Y. Zhang, X. Zhang, L. J. Zhang, J. Q. Wang, J. S. Hu, Z. D. Wei, L. J. Wan, Understanding the high activity of Fe-N-C electrocatalysts in oxygen reduction: Fe/Fe_3C nanoparticles boost the activity of Fe–N_x. *J. Am. Chem. Soc.* **138**, 3570–3578 (2016).
12. M. Lefevre, E. Proietti, F. Jaouen, J.-P. Dodelet, Iron-based catalysts with improved oxygen reduction activity in polymer electrolyte fuel cells. *Science* **324**, 71–74 (2009).
13. X. F. Li, Q. K. Li, J. Cheng, L. L. Liu, Q. Yan, Y. C. Wu, X. H. Zhang, Z. Y. Wang, Q. Qiu, Y. Luo, Conversion of dinitrogen to ammonia by FeN_3-embedded graphene. *J. Am. Chem. Soc.* **138**, 8706–8709 (2016).
14. W. G. Liu, L. L. Zhang, W. S. Yan, X. Y. Liu, X. F. Yang, S. Miao, W. T. Wang, A. Q. Wang, T. Zhang, Single-atom dispersed Co-N-C catalyst: Structure identification and performance for hydrogenative coupling of nitroarenes. *Chem. Sci.* **7**, 5758–5764 (2016).
15. G. Wu, K. L. More, C. M. Johnston, P. Zelenay, High-performance electrocatalysts for oxygen reduction derived from polyaniline, iron, and cobalt. *Science* **332**, 443–447 (2011).
16. J. N. Guo, C.-Y. Lin, Z. Xia, Z. Xiang, A pyrolysis-free covalent organic polymer for oxygen reduction. *Angew. Chem. Int. Ed.* **57**, 12567–12572 (2018).
17. Y. J. Sa, D. J. Seo, J. Woo, J. T. Lim, J. Y. Cheon, S. Y. Yang, J. M. Lee, D. Kang, T. J. Shin, H. S. Shin, H. Y. Jeong, C. S. Kim, M. G. Kim, T. Y. Kim, S. H. Joo, A general approach to preferential formation of active Fe–N_x sites in Fe-N/C electrocatalysts for efficient oxygen reduction reaction. *J. Am. Chem. Soc.* **138**, 15046–15056 (2016).
18. X. Wang, W. Chen, L. Zhang, T. Yao, W. Liu, Y. Lin, H. X. Ju, J. C. Dong, L. R. Zheng, W. S. Yan, X. S. Zheng, Z. J. Li, X. Q. Wang, J. Yang, D. S. He, Y. Wang, Z. X. Deng, Y. E. Wu, Y. D. Li, Uncoordinated amine groups of metal-organic frameworks to anchor single Ru sites as chemoselective catalysts toward the hydrogenation of quinoline. *J. Am. Chem. Soc.* **139**, 9419–9422 (2017).
19. Z. P. Zhang, J. T. Sun, F. Wang, L. M. Dai, Efficient oxygen reduction reaction (ORR) catalysts based on single iron atoms dispersed on a hierarchically structured porous carbon framework. *Angew. Chem. Int. Ed.* **57**, 9038–9043 (2018).
20. C. M. Zhao, X. Y. Dai, T. Yao, W. X. Chen, X. Q. Wang, J. Wang, J. Yang, S. Q. Wei, Y. E. Wu, Y. D. Li, Ionic exchange of metal organic frameworks to access single nickel sites for efficient electroreduction of CO_2. *J. Am. Chem. Soc.* **139**, 8078–8081 (2017).
21. Y. Chen, S. Ji, C. Chen, Q. Peng, D. Wang, Y. Li, Single-atom catalysts: Synthetic strategies and electrochemical applications. *Joule* **2**, 1242–1264 (2018).

22. P. Peng, Z. H. Zhou, J. Guo, Z. Xiang, Well-defined 2D covalent organic polymers for energy electrocatalysis. *ACS Energy Lett.* **2**, 1308–1314 (2017).
23. Z. Xiang, Y. Xue, D. Cao, L. Huang, J.-F. Chen, L. Dai, Highly efficient electrocatalysts for oxygen reduction based on 2D covalent organic polymers complexed with non-precious metals. *Angew. Chem. Int. Ed.* **53**, 2433–2437 (2014).
24. P. Yin, T. Yao, Y. Wu, L. Zheng, Y. Lin, W. Liu, H. Ju, J. F. Zhu, X. Hong, Z. Deng, G. Zhou, S. Wei, Y. Li, Single cobalt atoms with precise N-coordination as superior oxygen reduction reaction catalysts. *Angew. Chem. Int. Ed.* **55**, 10800–10805 (2016).
25. H. G. Zhang, S. Hwang, M. Y. Wang, Z. X. Feng, S. Karakalos, L. L. Luo, Z. Qiao, X. H. Xie, C. M. Wang, D. Su, Y. Y. Shao, G. Wu, Single atomic iron catalysts for oxygen reduction in acidic media: Particle size control and thermal activation. *J. Am. Chem. Soc.* **139**, 14143–14149 (2017).
26. G. Vile, D. Albani, M. Nachtegaal, Z. P. Chen, D. Dontsova, M. Antonietti, N. López, J. Pérez-Ramírez, A stable single-site palladium catalyst for hydrogenations. *Angew. Chem. Int. Ed.* **54**, 11265–11269 (2015).
27. Z. Li, D. Wang, Y. Wu, Y. Li, Recent advances in the precise control of isolated single-site catalysts by chemical methods. *Natl. Sci. Rev.* **5**, 673–689 (2018).
28. X. Wang, W. Wang, M. Qiao, G. Wu, W. Chen, T. Yuan, Q. Xu, M. Chen, Y. Zhang, X. Wang, J. Wang, J. Ge, X. Hong, Y. Li, Y. Wu, Y. Li, Atomically dispersed Au_1 catalyst towards efficient electrochemical synthesis of ammonia. *Sci. Bull.* **63**, 1246–1253 (2018).
29. P. Peng, L. Shi, F. Huo, S. J. Zhang, C. X. Mi, Y. H. Cheng, Z. H. Xiang, In situ charge exfoliated soluble covalent organic framework directly used for Zn-air flow battery. *ACS Nano* **13**, 878–884 (2019).
30. J. Y. Cheon, J. H. Kim, J. H. Kim, K. C. Goddeti, J. Y. Park, S. H. Joo, Intrinsic relationship between enhanced oxygen reduction reaction activity and nanoscale work function of doped carbons. *J. Am. Chem. Soc.* **136**, 8875–8878 (2014).
31. H. B. Yang, J. Miao, S.-F. Hung, J. Z. Chen, H. B. Tao, X. Z. Wang, L. P. Zhang, R. Chen, J. J. Gao, H. M. Chen, L. M. Dai, B. Liu, Identification of catalytic sites for oxygen reduction and oxygen evolution in N-doped graphene materials: Development of highly efficient metal-free bifunctional electrocatalyst. *Sci. Adv.* **2**, e1501122 (2016).
32. M. Piana, S. Catanorchi, H. A. Gasteiger, in *Proton Exchange Membrane Fuel Cells 8, Pts 1 and 2,* T. Fuller *et al.*, Eds. (Electrochemical Society Inc., 2008), vol. 16, pp. 2045–2055.
33. J. Suntivich, H. A. Gasteiger, N. Yabuuchi, Y. Shao-Horn, Electrocatalytic measurement methodology of oxide catalysts using a thin-film rotating disk electrode. *J. Electrochem. Soc.* **157**, B1263–B1268 (2010).
34. M. Nesselberger, S. Ashton, J. C. Meier, I. Katsounaros, K. J. J. Mayrhofer, M. Arenz, The particle size effect on the oxygen reduction reaction activity of Pt catalysts: Influence of electrolyte and relation to single crystal models. *J. Am. Chem. Soc.* **133**, 17428–17433 (2011).
35. S. Y. Wang, D. S. Yu, L. M. Dai, D. W. Chang, J. B. Baek, Polyelectrolyte-functionalized graphene as metal-free electrocatalysts for oxygen reduction. *ACS Nano* **5**, 6202–6209 (2011).
36. J. Wang, W. Liu, G. Luo, Z. J. Li, C. Zhao, H. R. Zhang, M. Z. Zhu, Q. Xu, X. Q. Wang, C. M. Zhao, Y. T. Qu, Z. K. Yang, T. Yao, Y. F. Li, Y. Lin, Y. Wu, Y. D. Li, Synergistic effect of well-defined dual sites boosting the oxygen reduction reaction. *Energy Environ. Sci.* **11**, 3375–3379 (2018).
37. Y. Qu, Z. J. Li, W. X. Chen, Y. Lin, T. W. Yuan, Z. K. Yang, C. M. Zhao, J. Wang, C. Zhao, X. Wang, F. Y. Zhou, Z. B. Zhuang, Y. Wu, Y. D. Li, Direct transformation of bulk copper into copper single sites via emitting and trapping of atoms. *Nat. Catal.* **1**, 781–786 (2018).
38. K. L. Wu, X. Chen, S. J. Liu, Y. Pan, W. C. Cheong, W. Zhu, X. Cao, R. A. Shen, W. X. Chen, J. Luo, W. S. Yan, L. R. Zheng, Z. Chen, D. S. Wang, Q. Peng, C. Chen, Y. D. Li, Porphyrin-like $Fe-N_4$ sites with sulfur adjustment on hierarchical porous carbon for different rate-determining steps in oxygen reduction reaction. *Nano Res.* **11**, 6260–6269 (2018).
39. Y. H. Han, Y. G. Wang, R. R. Xu, W. X. Chen, L. R. Zheng, A. J. Han, Y. Q. Zhu, J. Zhang, H. B. Zhang, J. Luo, C. Chen, Q. Peng, D. S. Wang, Y. D. Li, Electronic structure engineering to boost oxygen reduction activity by controlling the coordination of the central metal. *Energ. Environ. Sci.* **11**, 2348–2352 (2018).
40. Q. Q. Cheng, L. J. Yang, L. L. Zou, Z. Q. Zou, C. Chen, Z. Hu, H. Yang, Single cobalt atom and N codoped carbon nanofibers as highly durable electrocatalyst for oxygen reduction reaction. *ACS Catal.* **7**, 6864–6871 (2017).
41. J. P. Wang, G. K. Han, L. G. Wang, L. Du, G. Y. Chen, Y. Z. Gao, Y. L. Ma, C. Y. Du, X. Q. Cheng, P. J. Zuo, G. P. Yin, ZIF-8 with ferrocene encapsulated: A promising precursor to single-atom Fe embedded nitrogen-doped carbon as highly efficient catalyst for oxygen electroreduction. *Small* **14**, 1704282 (2018).
42. Z. P. Zhang, M. L. Dou, H. J. Liu, L. M. Dai, F. Wang, A facile route to bimetal and nitrogen-codoped 3D porous graphitic carbon networks for efficient oxygen reduction. *Small* **12**, 4193–4199 (2016).
43. Z. L. Wang, D. Xu, H. X. Zhong, J. Wang, F. L. Meng, X. B. Zhang, Gelatin-derived sustainable carbon-based functional materials for energy conversion and storage with controllability of structure and component. *Sci. Adv.* **1**, e1400035 (2015).
44. Y. Pan, S. J. Liu, K. A. Sun, X. Chen, B. Wang, K. L. Wu, X. Cao, W. C. Cheong, R. G. Shen, A. J. Han, Z. Chen, L. R. Zheng, J. Luo, Y. Lin, Y. Q. Liu, D. S. Wang, Q. Peng, Q. Zhang, C. Chen, Y. D. Li, A bimetallic Zn/Fe polyphthalocyanine-derived single-atom $Fe-N_4$ catalytic site: A superior trifunctional catalyst for overall water splitting and Zn-air batteries. *Angew. Chem. Int. Ed.* **57**, 8614–8618 (2018).
45. G. Liu, J. Li, J. Fu, G. Jiang, G. Lui, D. Luo, Y. P. Deng, J. Zhang, Z. P. Cano, A. Yu, D. Su, Z. Bai, L. Yang, Z. Chen, An oxygen-vacancy-rich semiconductor-supported bifunctional catalyst for efficient and stable zinc–air batteries. *Adv. Mater.* **31**, 1806761 (2019).
46. J. Han, X. Meng, L. Lu, J. Bian, Z. Li, C. Sun, Single-atom $Fe-N_x-C$ as an efficient electrocatalyst for zinc–air batteries. *Adv. Funct. Mater.* **2019**, 1808872 (2019).
47. Y. Qin, H.-H. Wu, L. A. Zhang, X. Zhou, Y. F. Bu, W. Zhang, F. Q. Chu, Y. T. Li, Y. Kong, Q. Zhang, D. B. Ding, Y. X. Tao, Y. X. Li, M. L. Liu, X. C. Zeng, Aluminum and nitrogen codoped graphene: Highly active and durable electrocatalyst for oxygen reduction reaction. *ACS Catal.* **9**, 610–619 (2019).
48. T. Wang, Z. K. Kou, S. C. Mu, J. P. Liu, D. P. He, I. S. Amiinu, W. Meng, K. Zhou, Z. X. Luo, S. Chaemchuen, F. Verpoort, 2D dual-metal Zeolitic-Imidazolate-Framework-(ZIF)-derived bifunctional air electrodes with ultrahigh electrochemical properties for rechargeable zinc–air batteries. *Adv. Funct. Mater.* **28**, 1705048 (2018).
49. S. Li, C. Cheng, X. J. Zhao, J. Schmidt, A. Thomas, Active salt/silica-templated 2D mesoporous $FeCo-N_x$-carbon as bifunctional oxygen electrodes for zinc-air batteries. *Angew. Chem. Int. Ed.* **57**, 1856–1862 (2018).
50. Z. H. Wang, H. H. Jin, T. Meng, K. Liao, W. Q. Meng, J. L. Yang, D. P. He, Y. L. Xiong, S. C. Mu, Fe, Cu-coordinated ZIF-derived carbon framework for efficient oxygen reduction reaction and zinc-air batteries. *Adv. Funct. Mater.* **28**, 1802596 (2018).
51. J. Guo, X. M. Yan, Q. Liu, Q. Li, X. Xu, L. T. Kang, Z. M. Cao, G. L. Chai, J. Chen, Y. B. Wang, J. N. Yao, The synthesis and synergistic catalysis of iron phthalocyanine and its graphene-based axial complex for enhanced oxygen reduction. *Nano Energy* **46**, 347–355 (2018).
52. H. H. Jin, H. Zhou, W. Q. Li, Z. H. Wang, J. L. Yang, Y. L. Xiong, D. P. He, L. Chen, S. C. Mu, In situ derived Fe/N/S-codoped carbon nanotubes from ZIF-8 crystals as efficient electrocatalysts for the oxygen reduction reaction and zinc–air batteries. *J. Mater. Chem. A* **6**, 20093–20099 (2018).
53. H.-F. Wang, C. Tang, B. Wang, B.-Q. Li, Q. Zhang, Bifunctional transition metal hydroxysulfides: Room-temperature sulfurization and their applications in Zn–air batteries. *Adv. Mater.* **29**, 1702327 (2017).

Acknowledgments: We thank L. Dai from Case Western Reserve University and J.-F. Chen and D. Cao at Beijing University of Chemical Technology for helpful discussion and suggestions; Z. Wen from Fujian Institute of Research on the Structure of Matter, Chinese Academy of Sciences for the fitting and analysis of the XAFS results; and the 1W1B station for XAFS measurements in Beijing Synchrotron Radiation Facility (BSRF). **Funding**: This work was supported by the National Key Research and Development Program of China (2017YFA0206500), the Natural Science Foundation of China (21676020 and 21606232), the Beijing Natural Science Foundation (17L20060), the Fundamental Research Funds for the Central Universities (buctrc201420 and buctrc201714), the BUCT Fund for Disciplines Construction and Development (XK1502), the Young Elite Scientists Sponsorship Program by CAST (2017QNRC001), the Talent cultivation and open project (OIC-201801007) of State Key Laboratory of Organic-Inorganic Composites, the Distinguished Scientist Program at BUCT (buctylkxj02), and the "111" Project of China (B14004). **Author contributions:** P.P., L.S., and C.M. performed synthesis, structural characterizations, electrochemical tests, and Zn-Air battery tests. P.P. and Z.X. wrote this paper. F.H., X.W., and S.Z. performed DFT calculations. Z.X. supervised and led this project. All authors provided critical feedback, helped shape the research and manuscript, and commented on the manuscript. **Competing interests:** The authors declare that they have no competing interests. **Data and materials availability:** All data needed to evaluate the conclusions in the paper are present in the paper and/or the Supplementary Materials. Additional data related to this paper may be requested from the authors.

Submitted 30 November 2018
Accepted 27 June 2019
Published 2 August 2019
10.1126/sciadv.aaw2322

Citation: P. Peng, L. Shi, F. Huo, C. Mi, X. Wu, S. Zhang, Z. Xiang, A pyrolysis-free path toward superiorly catalytic nitrogen-coordinated single atom. *Sci. Adv.* **5**, eaaw2322 (2019).

ScienceAdvances

A pyrolysis-free path toward superiorly catalytic nitrogen-coordinated single atom

Peng PengLei ShiFeng HuoChunxia MiXiaohong WuSuojiang ZhangZhonghua Xiang

Sci. Adv., 5 (8), eaaw2322. • DOI: 10.1126/sciadv.aaw2322

Science Advances (ISSN 2375-2548) is published by the American Association for the Advancement of Science. 1200 New York Avenue NW, Washington, DC 20005. The title *Science Advances* is a registered trademark of AAAS.